Particle-scale mechanics of sand crushing in compression and shearing using DEM

Particle-scale mechanics of sand crushing in compression and shearing using DEM

Kevin J. Hanley[1*], Catherine O'Sullivan[2], Xin Huang[3,4†]

[1] Institute for Infrastructure and Environment, School of Engineering, The University of Edinburgh, Edinburgh EH9 3JL, United Kingdom

[2] Department of Civil and Environmental Engineering, Skempton Building, Imperial College London, London SW7 2AZ, United Kingdom

[3] Department of Geotechnical Engineering, School of Civil Engineering, Tongji University, Shanghai 200092, China

[4] Key Laboratory of Geotechnical Engineering, Tongji University, Shanghai 200092, China

Key words: particle crushing, discrete element modelling, numerical simulation, critical state, relative breakage, coordination number, LAMMPS, high-performance computing, contact number ratio

IGC: D6/E13

Abstract

In this paper, the discrete element method is used to explore why differing amounts of breakage, quantified using Hardin's relative breakage parameter (B_r), are associated with the critical state line (CSL) and the normal compression line (NCL) at similar stress levels. Virtual samples initially containing more than 20,000 spherical particles were isotropically compressed to a range of confining pressures up to 56 MPa and subjected to triaxial compression, both considering and disregarding particle crushing. A particle crushing model was developed for these simulations which is both computationally tractable and gives macro-scale results qualitatively in agreement with laboratory tests. The CSLs are both linear in q–p'

[*] Formerly affiliation 2

[†] Formerly affiliation 2 and 'Department of Civil and Environmental Engineering, Haking Wong Building, The University of Hong Kong, Pokfulam Road, Hong Kong, China'

space. A curved peak envelope, corresponding to a curved Mohr–Coulomb envelope, is obtained for the crushing simulations which is absent when crushing is disabled. Consideration of particle crushing reduces the peak stresses and the volumetric response is much more contractive with crushing at high p'. These simulations capture the behaviour in B_r–p' space expected from published laboratory tests. The difference in behaviour along the NCL and CSL is explained by the larger fluctuations of contact force during triaxial shearing than during isotropic compression which was quantified using a newly-defined measure, contact number ratio. Particle crushing continues after the critical state is attained, contributing to counteract the dilation induced by particle rearrangement.

Introduction

Although it is not always quantified, it is almost inevitable that some particle crushing will occur during laboratory testing of sand. This is the case even when strong sand particles such as silica sands are compressed or sheared (Altuhafi and Coop, 2011): for example, Luzzani and Coop (2002) found that a small amount of breakage occurred when a Leighton Buzzard sand was subjected to low stress levels (≤ 100 kPa). Changes in the particle size distribution will influence soil properties, e.g., sample permeability will be reduced (Marketos and Bolton, 2007). When large stresses are attained, and consequently major changes occur in the particle size distribution due to crushing, the position of the critical state line is affected (Cheng et al., 2005; Muir Wood and Maeda, 2008; Bandini and Coop, 2011). Indeed, Coop et al. (2004) stated that when a constant volume is achieved in triaxial tests on crushable sands, the apparent critical state may be "a result of counteracting dilative strains from particle rearrangement and compressive strains from particle breakage". At the particle scale, breakage affects the transmission of forces through a granular medium.

The importance of grain crushing has led researchers using discrete element modelling (DEM) to incorporate various crushing models into their simulations of sands. The different models which have been used can be divided into two broad categories following the approach of McDowell and de Bono (2013):

1. Agglomerates are used in the simulation, created by joining the fundamental particles with bonds possessing finite strengths. The fundamental particles themselves are unbreakable and agglomerate crushing is simulated by bond failure.
2. The fundamental particles themselves are deemed to fail when a pre-allocated measure of strength is reached.

The first approach has been used quite widely (e.g., Robertson and Bolton, 2001; McDowell and Harireche, 2002; Cheng et al., 2003; Bolton et al., 2008; Cil and Alshibli, 2012; Wang and Yan, 2013). Its main disadvantage is the number of particles which must be simulated is necessarily large as the force and integration calculations must be done for each fundamental particle comprising the agglomerate rather than for the agglomerate as a whole. As large DEM samples are used in this research, the second approach was adopted. When using this approach, it is necessary to determine whether or not a particle has failed using some predefined criterion based on force or stress. If particles are deemed to have failed, a range of possible actions have been adopted in the literature. The simplest option is to delete the crushed particle (Marketos and Bolton, 2007) although this can lead to large losses of solid volume. More commonly, the crushed parent particle is replaced by multiple smaller daughter particles; these approaches can conserve volume (Ben-Nun and Einav, 2010; McDowell and de Bono, 2013) or not (Lobo-Guerrero and Vallejo, 2005a; Marketos and Bolton, 2009).

Some prior research has investigated the critical-state behaviour of crushable granular soils using DEM. Cheng et al. (2005) conducted constant-p' and constant-volume shearing simulations using around 400 bonded agglomerates bounded by rigid walls. They were unable to identify the exact location of the ultimate critical-state line (CSL) due to ongoing particle crushing and their simulations did not attain a constant void ratio even at 60% strain. The same authors previously showed good quantitative agreement with experimental data for a silica sand using similar simulations (Cheng et al., 2003), and showed the evolution of micro-mechanical parameters, such as coordination number and deviator fabric, in triaxial compression simulations of analogue sands comprising crushable agglomerates (Bolton et al., 2008). Normal compression lines (NCLs) for sands have often been obtained using DEM simulations, e.g., McDowell and de Bono (2013).

Experiments show that much more particle crushing takes place during shearing than during isotropic compression at similar stress levels (Coop and Lee, 1993). Even though DEM has

been used to obtain critical state and normal compression lines for virtual samples, a micro-mechanical explanation for the increased particle breakage during shearing is not available in the literature. One hypothesis is that the increased relative motion of particles during shearing compared with isotropic loading causes more variability in interparticle contact forces even though the mean stresses may be identical. Some evidence supporting this hypothesis is provided by Cheng et al. (2003) who suggested that large stress fluctuations, which are more likely to occur during shearing than isotropic compression, may cause failure of some agglomerates. Miao and Airey (2013) compared the steady-state gradings of a carbonate sand following both compression and shear in laboratory tests. They obtained a finer steady-state grading in shear and proposed that particle orientations in shear change more than in compression and hence contact stresses at steady state must be minimised at more particle orientations in shear than in isotropic compression where the particle orientations change comparatively little.

The main objective of this research is to explain conclusively why, at similar stress levels, differing amounts of breakage are associated with the CSL and the NCL by analysing the micro-mechanics of large-scale DEM simulations. To achieve this main aim, a crushing model has been developed for use in DEM simulations of sands which achieves a reasonable balance between the conflicting requirements of computational efficiency and physical appropriateness.

Development and implementation of crushing model

Requirements of a crushing model

For the purposes of this paper, the term ‘crushing model’ encompasses the failure criterion, the selection of appropriate input parameters and the action taken post-failure. Any such crushing model will have some deficiencies which is the inevitable consequence of having to

compromise the fidelity with which a crushing process is simulated for reasons of computational feasibility. Nonetheless, it is possible to identify a number of desirable attributes of a crushing model implemented in DEM:

- The macro-scale results of the simulation ought to be physically realistic when compared to laboratory data, at least qualitatively if not quantitatively.
- It should be possible to relate the parameters of the crushing model to physical measurements, i.e., the number of parameters which can be obtained only by calibration should be minimised.
- The model needs to be computationally efficient so that it may be used to investigate crushing in large samples. In practice, this requirement prevents the replacement of individual crushed particles with large numbers of smaller particles. Furthermore a lower bound is required on particle size as the critical time-step for stability of DEM simulations decreases with decreasing particle diameter (O'Sullivan and Bray, 2004). This bound can be linked to the physical concept of a comminution limit, with the caveat that specifying a finite comminution limit precludes development of a truly fractal ultimate grading (McDowell et al., 1996).
- Solid volume should be conserved.
- Some inherent variability is required in the crushing responses.
- A robust failure criterion is required for particles with multiple contacts. McDowell and de Bono (2013) explained why mean stress is a poor criterion, for example.
- The impact on fabric locally surrounding a crushed particle should be appropriate.

The crushing algorithm proposed here was developed considering these attributes and it is summarised in the flow chart presented in Fig. 1. Three key aspects of the model are discussed in detail below.

Failure criterion for particles

The failure criterion adopted for these simulations is based on the maximum force: particles are deemed to fail when a predefined contact force has been exceeded. This failure criterion has been used previously (Marketos and Bolton, 2007) and has some physical justification as the maximum contact force on a particle usually controls its failure (Russell et al., 2009). The failure criterion proposed by Christensen (2000) was also evaluated; it was found that using a per-particle stress tensor to compute the required stress invariants led to significant underpredictions of the extent of crushing (Hanley et al., 2014a). This prior study showed that while failure criteria based on contact force have some problems, this is also true of failure criteria based on 'average' particle stresses.

In each time-step and for each particle which has not reached the comminution limit, the largest contact force acting on the particle is compared to that particle's crushing force which is allocated as described below. In these simulations, the comminution limit, which is a numerical analogue of the physical limit discussed by Kendall (1978), was set at 120 μm: smaller than the diameter of the smallest particle present. The particle is deemed to fail if the contact force exceeds the crushing force, ignoring superposition of forces.

Estimation of particle crushing forces

The material simulated in this paper is a quartz sand. Nakata et al. (1999) provided experimental data for single-particle strain-controlled crushing tests of the quartz particle component of Aio sand using a particle size range of 0.85–2 mm subdivided into five size classes. Their data were analysed in terms of their characteristic particle strengths defined by Jaeger (1967):

$$\sigma = \frac{F}{d^2} \tag{1}$$

where F represents crushing force and d is the distance between the compression platens at the beginning of the crushing test. σ is a characteristic induced tensile stress within the loaded particle at failure. Nakata et al. (1999) made use of Weibull statistics to analyse their data, applying Eq. (2) to calculate the probability of survival, P_s, for particles of diameter d when subjected to a stress σ:

$$P_s(d) = e^{\left[-\left(\frac{d}{d_0}\right)^3\left(\frac{\sigma}{\sigma_0}\right)^m\right]} \tag{2}$$

In Eq. (2), m is the Weibull modulus and σ_0 represents the characteristic stress at which 37% of particles with the characteristic diameter d_0 survive. This equation has been used quite widely in geomechanics, e.g., McDowell and Bolton (1998). The force required to split the particle is taken as the crushing force for which values of m, σ_0 and d_0 are 4.2, 38 MPa and 1.29 mm, respectively (Nakata et al., 1999). Their results for compression of quartz particles of Aio sand (Fig. 2) show that $P_s(d)$ has an approximately linear relationship with σ and furthermore the plots of $P_s(d)$ against σ for five different size classes all coincide approximately (i.e., become independent of d) when the strength is normalised by the characteristic stress for particles of that diameter. An assumption made in this research, necessitated by a lack of experimental data, is that plots of $P_s(d)$ against σ have a similar appearance for particles smaller than 0.85 mm and hence the results in Fig. 2 are extrapolated for use in this study. The experimental data presented by Nakata et al. (1999) were also used by Wang and Yan (2013) in their DEM-based study of grain crushing.

The linear trendline illustrated in Fig. 2 has the form $P_s(d) = a\frac{\sigma}{\sigma_{0,d}} + b$, where a, the slope, is -1/1.45 ≈ -0.69; b, the intercept, is 1.7/1.45 ≈ 1.17, and $\sigma_{0,d}$ represents the characteristic

stress for particles of diameter d. This linear trendline is a function of $\sigma_{0,d}$ whereas Eq. (2) is a function of σ_0 so the equations are not in conflict. Both the linear trendline and Eq. (2) can be used to represent the data of Nakata et al. (1999). The approximation of Fig. 2 by a linear trendline is made for simplicity as it allows $P_s(d)$ to be substituted by $U(0,1)$: a random variate drawn from the uniform distribution:

$$\sigma = \sigma_{0,d} \frac{U(0,1) - b}{a} \tag{3}$$

Eq. (3) gives the characteristic strength of a particle of diameter d which contains an inherent variability due to the presence of a random variate. In order to use Eq. (3), the 37% characteristic stress for particles of diameter d must be known. Nakata et al. report that σ_0 is 38 MPa for particles in the range 1.18–1.4 mm (mean of 1.29 mm). These known values can be related to σ_0 for particles a and b of any diameter using Eq. (4) (Nakata et al., 1999):

$$\frac{\sigma_{0,a}}{\sigma_{0,b}} = \left(\frac{d_a}{d_b} \right)^{-\frac{3}{m}} \tag{4}$$

By combining Eq. (1), (3) and (4), Eq. (5) is obtained for the crushing force of particles of size d when compressed between horizontal platens:

$$F = \sigma_0 \frac{U(0,1) - b}{a} \left(\frac{d}{d_0} \right)^{-\frac{3}{m}} d^2 \tag{5}$$

For uniaxial compression of a single particle of diameter $d = d_0$ between rigid platens, the crushing force is 98 N, 62 N or 25 N for $U(0,1) = 0.1$, 0.5 or 0.9, respectively. $F \propto d^{\frac{2m-3}{m}}$ in Eq. (5) so the crushing force is independent of diameter if $m = 1.5$ and directly proportional to

the diameter if m = 3. Using m = 4.2 (Nakata et al., 1999), halving the particle diameter reduces its crushing force by a factor of 2.44 and increases its characteristic strength (Eq. (1)) by around 60% if everything else remains the same.

This Weibull modulus of 4.2 indicates that larger particles are capable of withstanding larger contact forces in uniaxial compression than smaller particles, on average. Larger particles are also more likely to participate in strong force chains (e.g., Voivret et al., 2009) and bear large contact forces. Therefore, there are two opposing effects determining particle survival: the largest particles, requiring the largest contact forces to induce failure, are subjected to the largest forces. This situation has interesting parallels with real polydisperse granular systems in which there are also opposing effects determining particle survival, although with different mechanisms. In reality, small particles contain fewer internal defects than large particles (Weibull, 1951) but also have fewer contacts with neighbouring particles giving them a more inhomogeneous internal stress state (McDowell and Bolton, 1998; Muir Wood and Maeda, 2008; Ben-Nun and Einav, 2010). In fact, the larger particles bear more of the load, on average, than the smaller ones. Take the 8 MPa simulation with crushing as an example and define 'small' particles as the smallest 20% of the particles (by number) and 'large' particles as the largest 20%. The mean normal contact force at the end of this simulation (once critical state had been attained) is 1.168 N for large—large contacts; 0.351 N for small—small contacts and 0.517 N for small—large contacts.

Post-failure operations

In the simulations presented here, instead of replacing the particle with an arrangement of smaller particles, its radius is reduced so that contact is lost with all neighbouring particles. This approach has a number of advantages: the number of particles does not increase greatly when extensive crushing occurs, the particle remains available to participate in the strong force network later in the simulation, it is computationally simple and there is an

instantaneous local decrease of stress which matches the observations of Nakata et al. (1999), albeit with lateral confinement in the simulation due to the surrounding particles. After the radius of a particle is reduced, the particle's crushing force is reallocated according to Eq. (5). Since the crushed particle should be more resilient than the parent, a restriction was imposed in the model to ensure that the crushing force cannot decrease post-crushing.

Unless particles are added to the simulation, the reduction of particle radii upon failure would cause a gradual loss of solid volume. This loss of solid volume would be unacceptable if extensive crushing were to occur. In these simulations, the change in solid volume is accumulated as V_a. When V_a exceeds the volume of one single particle with a diameter equal to the comminution limit of 120 μm (V_c), particles of volume V_c are successively added to the simulation, reducing V_a correspondingly, until $V_a < V_c$. As V_a is an accumulation of volumes of spherical shells for multiple particles, it is not associated with any one particle. Hence, the small particles added to the simulation are placed at randomly-selected locations within the sample, using a trial-and-error approach to ensure the particles are inserted into the void space without contacting any existing particles. If the amount of crushing is large, it may become impossible to add particles to the system without overlapping existing particles. In this case, rattlers are identified in the system, defined in this study as particles which have no contacts with neighbouring particles. Their diameters are increased by small increments to conserve solid volume. Two selected triaxial simulations were repeated without adjusting the rattler volumes to assess the sensitivity of the response to this assumption.

DEM simulations

The numerical samples used in this paper are approximately cubical and initially contain 22,246 spherical particles. When crushing is considered, the number of particles increases to more than 40,000 at the end of the shearing simulations at the highest σ_3'. The particle size distribution (PSD) before crushing is representative of the poorly-graded quartz Ham River

sand and is compared with the grading used by Coop and Lee (1993) on Fig. 3. The single-particle crushing behaviour of quartz particles of different sands, specifically Ham River sand and Aio sand, is assumed to be similar here. Some justification for this is provided by Coop and Lee (1993) who reported that the NCL for Ham River sand is very similar to those of two other quartz sands, Toyoura sand and Chatahoochee River sand, indicating similar crushing characteristics. Ham River sand has the same particle strength regardless of whether it is dry or saturated (Coop and Lee, 1995). Periodic boundary conditions were chosen to eliminate boundary effects (Huang et al., 2014a) and ensure a homogeneous deformation field (Cundall, 1988). The use of periodic boundaries means that shear bands are not developed in these simulations. The sample preparation methodology is described by Hanley et al. (2014b): a random number generator was used to place particles successively within a periodic cell without overlapping any pre-existing particles. Once all particles had been placed successfully within the periodic cell, a servo-control algorithm was used to shrink the cell until a predefined isotropic stress state had been attained and the sample was in a stable equilibrium.

A version of the open-source, MPI-parallelised code LAMMPS (Plimpton, 1995) was used which included some additions and modifications made by the authors. In particular, a stress-control algorithm for periodically-bounded samples and the crushing model described above were implemented and the interparticle contact models were modified substantially. A simplified Hertz-Mindlin contact model was used for these simulations with a shear modulus of 29.17 GPa and a Poisson's ratio of 0.2: realistic parameters for a quartz sand. Neither damping nor gravity were active during the triaxial compression simulations. Local damping (Potyondy and Cundall, 2004) was active during the isotropic compression phase with a damping coefficient of 0.2. The particle surface friction coefficient was zero during the sample preparation phase to create very dense samples; this was increased to 0.25 once isotropic compression was complete based on the numerical study of Huang et al. (2014b).

The time-step used was 8 ns, calculated by considering two contacting particles at the comminution limit with an interparticle overlap equal to 5% of the particle radii.

The implementation of the crushing model in LAMMPS was verified using small-scale idealised arrangements of fewer than 10 particles. Once the model had been verified, two separate sets of simulations were conducted: in one set, particle crushing was permitted up to the comminution limit whereas crushing was prevented in the second set. Initially isotropically-compressed samples at 1 MPa were created. The stable assemblies formed at the end of this procedure were in turn further isotropically compressed to 2, 4, 8, 16, 24, 32, 40 and 48 MPa. An isotropic 56 MPa sample was also created for the case without crushing. The upper limit of confining pressure was imposed because of the requirement for interparticle overlaps to remain small so that point contact is approximated (Potyondy and Cundall, 2004). For both the crushing and non-crushing cases, the isotropically-compressed samples at confining pressures between 1 and 40 MPa were subjected to drained (i.e., constant σ_3') triaxial compression in which each sample was sheared vertically in compression at a strain rate of 1 s^{-1} while the minor and intermediate principal effective stresses were held constant. Two additional triaxial simulations were run at confining pressures of 32 and 40 MPa in which the diameters of rattlers were not increased to conserve solid volume. The overall loss of solid volume was 0.9% and 6.2% for these respective simulations. All simulations were run using eight 24-core nodes of the UK national high-performance computing facility, ARCHER. The use of high-performance computing was essential to run these simulations: each stage of isotropic compression was run for between 8 and 24 hours while each triaxial shearing simulation required between 24 and 48 hours when crushing was considered (6–12 hours when crushing was disregarded).

Macro-scale results

Fig. 4(a) shows the evolution of stress ratio, q/p', against axial strain for the crushing simulations while Fig. 4(d) is the corresponding plot for the non-crushing simulations. Triaxial compression continued to 50% axial strain ensuring that a critical state was attained for all simulations except the crushing simulation at $\sigma_3' = 40$ MPa. All simulations attained a similar q/p' at the critical state of around 0.7 (shown by dashed lines) regardless of whether crushing is considered or not, although there is a wider dispersion about this critical state value for the crushing cases. In the absence of crushing, the peak stress ratio attained increases slightly with σ_3' particularly at low σ_3', becoming approximately constant at $\sigma_3' > 8$ MPa; this is no longer true when crushing is considered as the peak q/p' increases with σ_3' for $\sigma_3' \leq 8$ MPa but decreases thereafter. The corresponding stress paths are shown in Fig. 4(b) and Fig. 4(e) on which the peak and critical state envelopes are superimposed as dashed lines. A linear peak envelope gives an excellent description of the non-crushing data ($q = 1.073p'$ with $R^2 = 0.9999$, noting that $R^2 < 1$ because of the variation of peak q/p' with σ_3' for $\sigma_3' < 16$ MPa). A quadratic curve gives good agreement with the crushing data ($q = 1.036p' - 4.389 \times 10^{-6} p'^2$ with $R^2 = 0.9981$). As discussed by Tarantino and Hyde (2005), a curved peak envelope (i.e., a decrease in peak friction angle as p' increases), which corresponds to a curved Mohr–Coulomb envelope, has often been attributed to particle crushing effects. The absence of a curved peak envelope on Fig. 4(e) when crushing is disabled provides further evidence for this explanation. A similarly curved Mohr–Coulomb envelope was obtained by Lobo-Guerrero and Vallejo (2005b) in their 2D biaxial test simulations. The critical state envelopes are linear regardless of whether crushing is considered or not. Comparing Fig. 4(b) and Fig. 4(e) shows that consideration of particle crushing reduces the peak stresses. The use of periodic boundary conditions prevents the development of shear bands and hence limits the permissible failure modes. This may not have such a marked effect at high σ_3': Wang and Yan (2013) found that very high levels of particle breakage tend to suppress the development of shear bands in their simulations of crushable agglomerates. In addition, the relatively

homogeneous deformation field enables robust conclusions to be drawn on the material behaviour.

The volumetric strains are shown in Fig. 4(c) (crushing) and Fig. 4(f) (non-crushing). At low confining pressures, the samples contract slightly before dilating until critical state is attained at 20–25% axial strain, as expected for dense samples. Increasing the confining pressure causes the response to become more contractive. The effect of confining pressure on the volumetric response is small in the absence of crushing, but is much more significant when crushing takes place. At the highest σ_3' of 40 MPa, the volumetric strain remains positive (contractive) throughout shearing to 50% axial strain when crushing is considered and critical state is never reached. The 40 MPa simulation in which volume loss is permitted contracts monotonically, reaching a volumetric strain of around 5% at 50% axial strain. The large difference between the two 40 MPa simulations in terms of volumetric response (and both 32 MPa simulations, to a lesser extent) shows some sensitivity to the details of the crushing model implementation. The observation that crushing causes the response to become more contractive agrees with de Bono and McDowell (2014). The evolution of volumetric strains with and without grain crushing also agrees closely with the observations of Bolton et al. (2008). In their simulations, shear bands were also not developed and all samples dilated at confining pressures up to 40 MPa when crushing was prevented. However, the inclusion of crushing in the simulations of Bolton et al. (2008) also changed the behaviour from overall dilative to overall contractive.

Fig. 5 shows the CSLs and NCLs both with and without crushing in e–log(p') space. A large difference is seen in the critical-state void ratios at high p'; this is caused by the progressive reduction of the void volume by the addition of daughter particles to the void space when the crushing model is active. The relative positions of the CSLs for crushable and uncrushable particles presented by de Bono and McDowell (2014) in e–log(p') space correspond closely with those of this study; the physically-unrealistic increase of specific volume they obtained

at low p' in the absence of crushing can be attributed to their use of an interparticle friction coefficient of 0.5 (Huang et al., 2014b). The results at high p' also agree with Muir Wood and Maeda (2008) who found that the position of the CSL will move downwards as the range of particle sizes considered increases. The CSLs are presented in q–p' space on Fig. 6. The slope of the CSL, M_{cs}, is slightly higher when crushing is considered: 0.731 compared to 0.687 without crushing. The closeness of the responses in q–p' space is expected from experimental studies: Coop et al. (2004) found that particle breakage due to shearing had no significant effect on the mobilised angle of shearing resistance while Ventouras and Coop (2009) obtained identical CSLs in q–p' space regardless of fines content. Interestingly, de Bono and McDowell (2014) obtained substantially different results in q–p' space. When crushing was included, their CSL deviated markedly from linearity at large stresses although they show only four points, the samples were initially monodisperse and the states reached were not truly critical. When the loss of solid volume is permitted at high σ_3', the two additional points on Fig. 6 suggest that a curved, concave CSL would be obtained which is not physically realistic.

Li and Wang (1998) suggested plotting CSLs in e–$(p'/p_a)^{\alpha}$ space according to the following relationship:

$$e_{cs} = \Gamma - \lambda\left(\frac{p'_{cs}}{p_a}\right)^{\alpha} \tag{6}$$

where e_{cs} and p_{cs}' are the critical-state void ratios and mean effective stresses, respectively; λ and Γ are the slope and intercept of the CSL; p_a is atmospheric pressure (taken as 101.325 kPa here); α is a material constant often taken as 0.7 for quartz sands. The CSLs plotted using this convention are shown on Fig. 7. When crushing is not permitted, the data may be represented very well by a linear regression ($R^2 = 0.9975$; $\lambda = 8.513 \times 10^{-4}$; $\Gamma = 0.6003$). There is a marked concavity when crushing takes place which follows a quadratic regression ($R^2 = 0.9979$).

The differences between the critical state lines are due to the change in grading induced by particle crushing during shearing. Fig. 8 shows how the PSD of the simulated Ham River sand evolves due to this crushing; similar plots have been shown previously for DEM simulations including grain crushing, e.g., Cheng et al. (2005); Tarantino and Hyde (2005). Negligible crushing takes place below $\sigma_3' = 8$ MPa. As σ_3' increases, the distributions initially display the expected leftward shift as the diameters of large particles are reduced upon failure and fine particles at the comminution limit of 120 μm are added to the system. For σ_3' values beyond 24 MPa, the voids have been filled with debris to such an extent that it becomes impossible to add small particles to the system without overlaps to conserve volume. Instead, the diameters of rattlers, which are primarily small-diameter particles, are increased which causes the fraction of particles at the comminution limit to decrease beyond 24 MPa. This is illustrated clearly in Fig. 8(b). This approach to solid-volume conservation at high σ_3' has a smaller influence on the volumetric PSDs (Fig. 8(a)). The significant effect of this two-stage volume conservation approach on PSDs at high σ_3' is demonstrated by comparison with those two simulations, at 32 MPa and 40 MPa, for which rattler diameters are not increased and hence loss of solid volume occurs.

It can be difficult to judge the extent of crushing by visually comparing PSDs. Hardin (1985) proposed a method to quantify the amount of particle breakage by comparing the volume-based PSDs, as shown in Fig. 8(a), before and after testing. The measure defined by Hardin, relative breakage (B_r), is defined in Fig. 9(a). B_r was quantified at the end of each isotropic compression and triaxial shearing simulation conducted which considers particle crushing, taking Fig. 3 as the initial grading for calculation. These relative breakages are plotted against p' on Fig. 9(b). Far more crushing takes place at the critical state than under isotropic conditions at the same p'. These simulation results can be compared with experimental data for Ham River sand shown on Fig. 9(c) using data presented in Coop (2003) and Coop and Lee (1993). The CSLs in B_r–p' space are very similar qualitatively but considerably more

breakage is seen in the laboratory tests than the simulations. The marked shape difference between the real sand grains and the simulated perfect spheres may be the origin of this disparity: real particles can exert interlocking forces on each other which spheres cannot, for instance. These results qualitatively capture the relative positions and shapes of the NCL and CSL in B_r–p' space presented by Coop (2003) for a carbonate sand, Dog's Bay. Insufficient experimental data were available to allow comparison with Ham River sand as significant amounts of crushing during isotropic compression could be achieved only by using confining pressures in excess of the experimental capacity. Lobo-Guerrero and Vallejo (2005b) also found that much more crushing was observed when a deviator stress was imposed rather than isotropic stress conditions. The evolution of B_r with axial strain through triaxial shearing is shown in Fig. 10. For σ_3' values $\geq$ 8 MPa, particle crushing continues until the end of each simulation.

Micro-scale results

The simulations were run by isotropically compressing samples to progressively higher confining pressures, and then shearing the stable samples produced at each stage. This approach means that the force transmitted at any specific interparticle contact can be tracked throughout the simulations. Fig. 11 plots the contact force at regularly-spaced output intervals during isotropic compression and triaxial shearing for two randomly-selected, persistent contacts, noting that choosing different contacts would give similar results. On Fig. 11, there are two possibilities for the stable assembly (and hence two possibilities for each contact) produced by any isotropic compression stage: the assembly may be isotropically compressed to a higher confining pressure or else it may be sheared triaxially. The force invariably stabilises quickly during isotropic compression and remains constant thereafter until the confining pressure is increased. The small fluctuations in the contact force are primarily due to the number and distribution of crushing events. For example, only one particle was added during isotropic compression of the 8 MPa sample to 16 MPa. By comparison, more than

1700 particles were added when the same sample was sheared triaxially to 50% axial strain and particles continued to fail throughout the shearing process. The fluctuations in the contact force during triaxial shearing peak at more than 10 N for both contacts. Since it is sufficient for the contact force to exceed the crushing force allocated to either particle only instantaneously to induce failure, considerable crushing is caused by the peaks of these transient fluctuations exceeding the crushing force. The fact that this variability is absent during isotropic compression explains why more breakage occurs during shearing than during compression and hence why the CSL lies above the NCL on Fig. 9(b). Fig. 11 supports the suggestion of Cheng et al. (2003) that order-of-magnitude stress fluctuations crush some agglomerates.

A new quantity, *contact number ratio*, was defined which is capable of distinguishing the increased particle translational motion that occurs during shearing from that which occurs during isotropic compression. The contact number ratio, CNR, is defined as

$$CNR = \frac{C_d}{C_0} \tag{7}$$

where C_d is the total number of distinct contacts present during a simulation (either isotropic compression from a isotropic stress state to a higher confining pressure or triaxial compression of an isotropic assembly) and C_0 is the number of contacts present at the start of a simulation. Large values of CNR indicate that contacts are short-lived and there is increased particle motion in the assembly. As all simulations were run for similar times, the CNRs for isotropic compression and triaxial shearing may be reasonably compared. The CNRs for four simulations (isotropic compression of an 8 MPa sample to 16 MPa and triaxial shearing of the same 8 MPa sample, with and without crushing) are compared on Fig. 12.

For isotropic compression, the CNRs initially rise sharply but rapidly attain constant values. The particles in these assemblies are quickly locked into position by neighbouring particles in an isotropic fabric. The CNRs for triaxial shearing increase monotonically over time and are approximately double the CNRs for isotropic compression at the end of the simulations. The CNRs are larger when crushing is considered than when crushing is prevented. Similar trends can be seen on Fig. 13 in which the CNRs at the end of each simulation are compared. The final CNRs for isotropic compression are consistently far less than the values for triaxial shearing. In the absence of crushing, the CNRs for triaxial shearing decrease monotonically with increasing p': larger stresses lock particles in position more effectively than low stresses. When the amount of crushing is large, a lot of particle rearrangement takes place giving large CNR values.

Considerable insight can be gained by plotting the evolution of the standard coordination number (average number of contacts per particle) or mechanical coordination number (defined by Thornton (2000) as the average number of contacts per particle disregarding those with fewer than two contacts). For the crushing simulations, partial coordination numbers may additionally be calculated as has previously been done for coarse and fine fractions (Pinson et al., 1998; Minh and Cheng, 2013; Shire et al., 2014). We define parent particles as those 22,246 particles present from the beginning of isotropic compression, daughter particles as 120-μm-diameter fines added to the system during the simulation, crushed particles as all daughter particles and broken parent particles, and uncrushed particles as unbroken parent particles. Thus, six partial coordination numbers (parent–parent; parent–daughter; daughter–daughter; crushed–crushed; crushed–uncrushed; uncrushed–uncrushed) were calculated along with the standard and mechanical coordination numbers. It is noted that each triad of partial coordination numbers sum to give the standard coordination number. These eight coordination numbers are plotted against axial strain in Fig. 14 for σ_3' values of 8 MPa and 32 MPa. The mechanical coordination number decreases consistently with strain in both cases. The same is true for the uncrushed–uncrushed and parent–parent partial coordination

numbers: these decreasing trends are expected as the numbers of parent and uncrushed particles in the system cannot increase. The daughter–daughter partial coordination number remains low (< 0.2) even at σ_3' = 32 MPa, although this is, to some extent, a consequence of the method used to add daughter particles to the system and it is likely that changing this method would significantly affect the partial coordination numbers.

Fig. 4(a) and 4(c) show that both samples reach critical state before 35% axial strain; however Fig. 10 demonstrates that particles continue to fail at higher strain levels. This strongly supports the observation of Coop et al. (2004), based on ring shear tests of crushable sands, that an apparent critical state can be achieved which may be due to a balance between particle breakage, tending to cause sample contraction, and dilation induced by particle rearrangement. This follows the mechanism proposed by Chandler (1985) who stated that compression due to crushing and dilation due to particle rearrangement balance to give a constant volume response indicative of a critical state. Our data suggest that this is the case for the triaxial test simulations presented here. However, numerous physical experiments and DEM studies have demonstrated conclusively that a critical state can be attained in the absence of grain crushing. This critical state can only be caused by the attainment of a consistent assembly volume following particle rearrangements. This was investigated using the non-crushing simulation at σ_3' = 8 MPa. Voro++ (Rycroft, 2009) was used to quantify the volumes of the Voronoi cells associated with each particle at post-critical state axial strains of 30% and 50%. The volumes of individual cells changed considerably even though the total sample volume was invariant, i.e., local dilation at one point in the material was counteracted by contractive strains of similar magnitude at another point in the material. A similar continual redistribution of volumes locally within the sample occurs in systems comprising crushable particles, which may be explained by the ongoing development and collapse of strong force chains (Rechenmacher et al., 2010).

Conclusions

In this paper, a crushing model with some novel aspects has been described and the results of a set of large-scale isotropic compression and drained triaxial shearing simulations has been presented and discussed. The particle-scale mechanisms underlying prior macro-scale response observations in physical tests were explored. When crushing is considered, the volumetric response during shearing becomes much more contractive as the confining pressure is increased; this effect is comparatively small when crushing is disregarded. The CSLs in e–log(p') space with and without crushing diverge at large p' as the voids in the crushing simulations are progressively filled with debris. In q–p' space, the CSLs are both linear and M_{cs} is slightly higher when crushing is considered; however, this difference is not statistically significant. A curved peak envelope, indicating a curved Mohr–Coulomb envelope, was obtained for the crushing simulations compared with a linear peak envelope in the absence of crushing. Good qualitative agreement was obtained in terms of relative breakage (Hardin, 1985) when the simulation data and the experimental critical-state data for Ham River sand presented by Coop (2003) were compared. Furthermore, these simulations qualitatively capture the relative positions and shapes of the NCL and CSL in B_r–p' space for the carbonate Dog's Bay sand (Coop, 2003).

Much larger fluctuations of contact force are present during triaxial shearing than during isotropic compression, suggesting this is why shearing causes considerably more particle breakage. This was confirmed using a newly-defined measure, contact number ratio, which quantifies the number of contacts formed during a simulation. These ratios are much higher during shearing than compression. Particle crushing continues after reaching a constant volume which is an apparent critical state. This provides numerical evidence for the hypothesis of Coop et al. (2004) that the critical state observed in triaxial tests on crushable sands is a balance between particle breakage, tending to cause sample contraction, and dilation induced by particle rearrangement. The ongoing development and collapse of strong

force chains, causing a continual redistribution of volumes locally within the sample, is also likely to contribute to the attainment of the critical state in systems of crushable particles.

These computationally-demanding simulations were enabled by access to the UK national high-performance computing facility, ARCHER. The simulations described in this paper could not have been run feasibly using the single-processor DEM codes that remain popular among the geomechanics community. This provides a good example of the type of research that can be achieved using parallel codes on supercomputers.

Acknowledgments

K. Hanley would like to acknowledge funding from the Royal Commission for the Exhibition of 1851. Computational time on ARCHER was provided as part of Grant EP/I006761/1 from the Engineering and Physical Sciences Research Council.

References

Altuhafi, F. N. and Coop, M. R. (2011): Changes to particle characteristics associated with the compression of sands, *Géotechnique*, **61**(6), 459–471.

Bandini, V. and Coop, M. R. (2011): The influence of particle breakage on the location of the critical state line of sands, *Soils Found.*, **51**(4), 591–600.

Ben-Nun, O. and Einav, I. (2010): The role of self-organization during confined comminution of granular materials, *Phil. Trans. R. Soc. A*, **368**, 231–247.

Bolton, M. D., Nakata, Y. and Cheng, Y. P. (2008): Micro- and macro-mechanical behaviour of DEM crushable materials, *Géotechnique*, **58**(6), 471–480.

de Bono, J. P. and McDowell, G. R. (2014): DEM of triaxial tests on crushable sand, *Granul. Matter*, **16**(4), 551–562.

Chandler, H. W. (1985): A plasticity theory without Drucker's postulate, suitable for granular materials, *Journal of the Mechanics and Physics of Solids*, **33**(3), 215–226.

Cheng, Y. P., Nakata, Y. and Bolton, M. D. (2003): Discrete element simulation of crushable soil, *Géotechnique*, **53**(7), 633–641.

Cheng, Y. P., Bolton, M. D. and Nakata, Y. (2005): Grain crushing and critical states observed in DEM simulations, Powders and Grains 2005, *Proc. 5th Int. Conf. on Micromechanics of Granular Media*, Stuttgart, pp. 1393–1397.

Christensen, R. M. (2000): Yield functions, damage states, and intrinsic strength, *Math. Mech. Solids*, **5**, 285–300.

Cil, M. B. and Alshibli, K. A. (2012): 3D assessment of fracture of sand particles using discrete element method, *Géotechnique Lett.*, **2**, 161–166.

Coop, M. R. (2003): On the mechanics of reconstituted and natural sands. In *Deformation characteristics of geomaterials* (eds H. Di Benedetto, T. Doanh, H. Geoffroy and C. Sauéat), vol. **2**, pp. 29–58. Lisse: Swets and Zeitlinger.

Coop, M. R. and Lee, I. K. (1993): The behaviour of granular soils at elevated stresses, *Predictive soil mechanics: Proc. of the Wroth Memorial Symposium*, London, pp. 186–198.

Coop, M. R. and Lee, I. K. (1995): The influence of pore water on the mechanics of granular soils, *Proc. XI European Conf. Soil Mechs. Foundn. Engng.*, Copenhagen, pp. 1.63–1.72.

Coop, M. R., Sorensen, K. K., Bodas Freitas, T. and Georgoutsos, G. (2004): Particle breakage during shearing of carbonate sand, *Géotechnique*, **54**(3), 157–163.

Cundall, P. (1988): Computer simulations of dense sphere assemblies. In *Micromechanics of granular materials* (eds M. Satake, J. Jenkins), pp. 113–123. Amsterdam: Elsevier.

Hanley, K. J., O'Sullivan, C. and Huang, X. (2014): Investigation of Christensen's two-parameter failure criterion for brittle materials, *Proc. of the Int. Symposium on Geomechanics from Micro to Macro*, Cambridge, vol. **1**, pp. 129–134.

Hanley, K. J., Huang, X., O'Sullivan, C. and Kwok, F. C. Y. (2014): Temporal variation of contact networks in granular materials, *Granul. Matter*, **16**(1), 41–54.

Hardin, B. O. (1985): Crushing of soil particles, *J. Geotech. Engng.*, **111**(10), 1177–1192.

Huang, X., Hanley, K. J., O'Sullivan, C. and Kwok, F. C. Y. (2014): Effect of sample size on the response of DEM samples with a realistic grading, *Particuology*, **15**, 107–115.

Huang, X., Hanley, K. J., O'Sullivan, C. and Kwok, C. Y. (2014): Exploring the influence of interparticle friction on critical state behaviour using DEM, *Int. J. Numer. Anal. Met.*, **38**(12), 1276–1297.

Jaeger, J. C. (1967): Failure of rocks under tensile conditions, *Int. J. Rock Mech. Min. Sci.*, **4**(2), 219–227.

Kendall, K. (1978): The impossibility of comminuting small particles by compression, *Nature*, **272**, 710–711.

Li, X. S. and Wang, Y. (1998): Linear representation of steady-state line for sand, *J. Geotech. Geoenviron. Eng.*, **124**, 1215–1217.

Lobo-Guerrero, S. and Vallejo, L. E. (2005): Crushing a weak granular material: experimental numerical analyses, *Géotechnique*, **55**(3), 245–249.

Lobo-Guerrero, S. and Vallejo, L. E. (2005): Analysis of crushing of granular material under isotropic and biaxial stress conditions, *Soils Found.*, **45**(4), 79–87.

Luzzani, L. and Coop, M. R. (2002): On the relationship between particle breakage and the critical state line of sands, *Soils Found.*, **42**(2), 71–82.

Marketos, G. and Bolton, M. D. (2007): Quantifying the extent of crushing in granular materials: A probability-based predictive method, *J. Mech. Phys. Solids*, **55**, 2142–2156.

Marketos, G. and Bolton, M. D. (2009): Compaction bands simulated in discrete element models, *J. Struct. Geol.*, **31**, 479–490.

McDowell, G. R. and Bolton, M. D. (1998): On the micromechanics of crushable aggregates, *Géotechnique*, **48**(5), 667–679.

McDowell, G. R., Bolton, M. D. and Robertson, D. (1996): The fractal crushing of granular materials, *J. Mech. Phys. Solids*, **44**(12), 2079–2101.

McDowell, G. R. and de Bono, J. P. (2013): On the micro mechanics of one-dimensional normal compression, *Géotechnique*, **63**(11), 895–908.

McDowell, G. R. and Harireche, O. (2002): Discrete element modelling of yielding and normal compression of sand, *Géotechnique*, **52**(4), 299–304.

Miao, G. and Airey, D. (2013): Breakage and ultimate states for a carbonate sand, *Géotechnique*, **63**(14), 1221–1229.

Minh, N. H. and Cheng, Y. P. (2013): A DEM investigation of the effect of particle-size distribution on one-dimensional compression, *Géotechnique*, **63**(1), 44–53.

Muir Wood, D. and Maeda, K. (2008): Changing grading of soil: effect on critical states, *Acta Geotechnica*, **3**(1), 3–14.

Nakata, Y., Hyde, A. F. L., Hyodo, M. and Murata, H. (1999): A probabilistic approach to sand particle crushing in the triaxial test, *Géotechnique*, **49**(5), 567–583.

O'Sullivan, C. and Bray, J. D. (2004): Selecting a suitable time step for discrete element simulations that use the central difference time integration scheme, *Eng. Computation.*, **21**(2/3/4), 278–303.

Pinson, D., Zou, R. P., Yu, A. B., Zulli, P. and McCarthy, M. J. (1998): Coordination number of binary mixtures of spheres, *J. Phys. D Appl. Phys.*, **31**(4), 457–462.

Plimpton, S. (1995): Fast parallel algorithms for short-range molecular dynamics, *J. Comput. Phys.*, **117**, 1–19.

Potyondy, D. O. and Cundall, P. A. (2004): A bonded-particle model for rock, *Int. J. Rock Mech. Min. Sci.*, **41**(8), 1329–1364.

Rechenmacher, A, Abedi, S. and Chupin, O. (2010): Evolution of force chains in shear bands in sands, *Géotechnique*, **60**(5), 343–351.

Robertson, D. and Bolton, M. D. (2001): DEM simulation of crushable grains and soils, *Proc. Powder and Grains*, Sendai, pp. 623–626.

Russell, A. R., Muir Wood, D. and Kikumoto, M. (2009): Crushing of particles in idealised granular assemblies, *J. Mech. Phys. Solids*, **57**, 1293–1313.

Rycroft, C. H. (2009): Voro++: A three-dimensional Voronoi cell library in C++, *Chaos*, **19**, 041111.

Shire, T., O'Sullivan, C., Hanley, K. J. and Fannin, R. J. (2014): Fabric and effective stress distribution in internally unstable soils, *J. Geotech. Geoenviron*. **140**(12), 04014072.

Tarantino, A. and Hyde, A. F. L. (2005): An experimental investigation of work dissipation in crushable materials, *Géotechnique*, **55**(8), 575–584.

Thornton, C. (2000): Numerical simulations of deviatoric shear deformation of granular media, *Géotechnique*, **50**(1), 43–53.

Ventouras, K. and Coop, M. R. (2009): On the behaviour of Thanet Sand: an example of an uncemented natural sand, *Géotechnique*, **59**(9), 727–738.

Voivret, C., Radjaï, F., Delenne, J.-Y. and El Youssoufi, M. S. (2009): Multiscale force networks in highly polydisperse granular media, *Phys. Rev. Lett.*, **102**, 178001.

Wang, J. and Yan, H. (2013): On the role of particle breakage in the shear failure behavior of granular soils by DEM, *Int. J. Numer. Anal. Met.*, **37**(8), 832–854.

Weibull, W. (1951): A statistical distribution function of wide applicability, *J. Appl. Mech.*, **18**, 293–297.

Figures

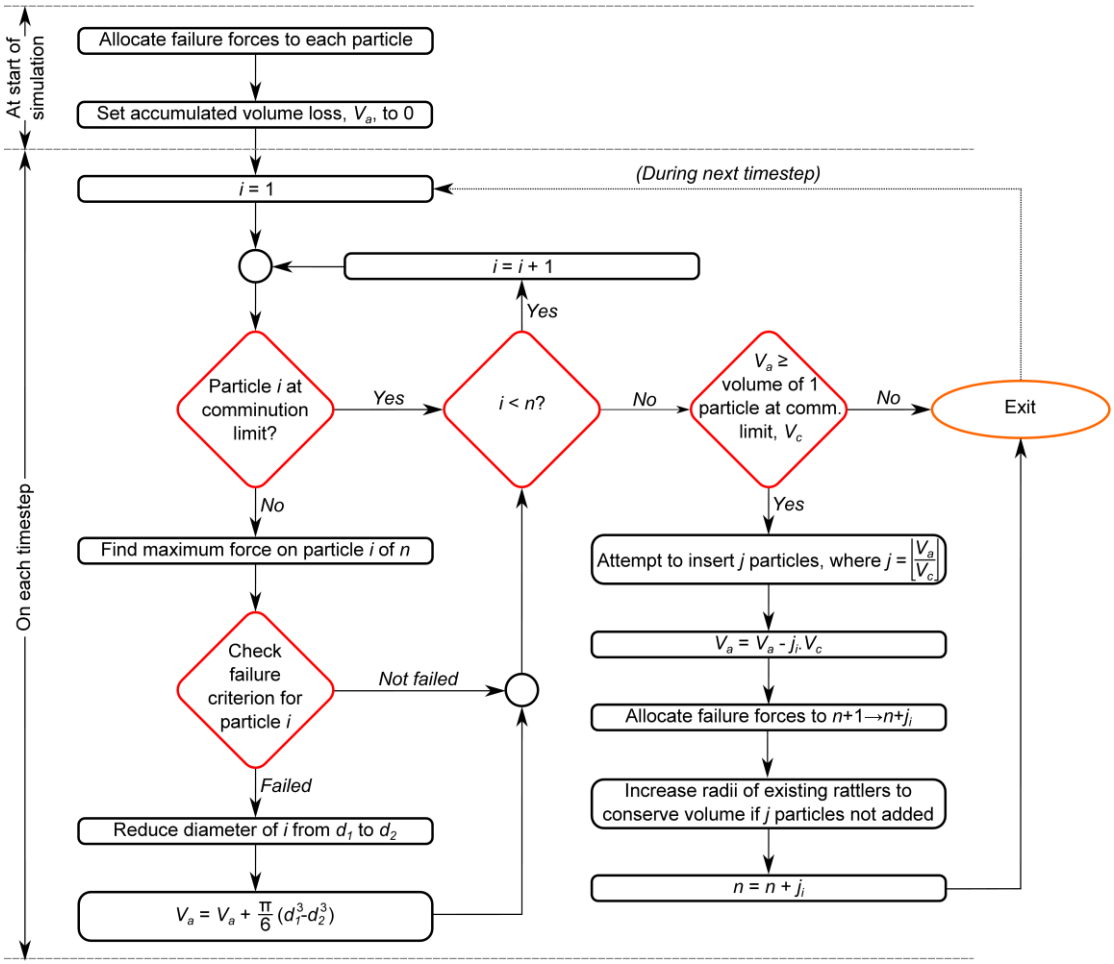

Figure 1 Flowchart showing the implementation of the crushing model in a DEM code

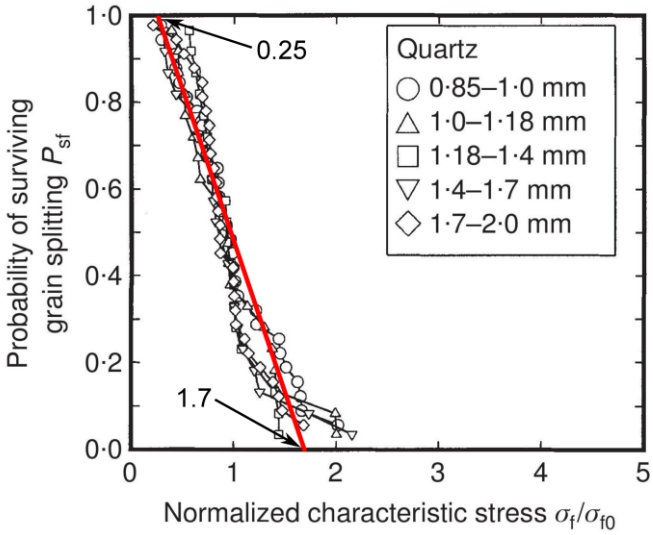

Figure 2 Survival probability plotted against the stress normalised by the 37% characteristic stress for quartz particles of Aio sand, adapted from Nakata et al. (1999) to include an approximate linear trendline

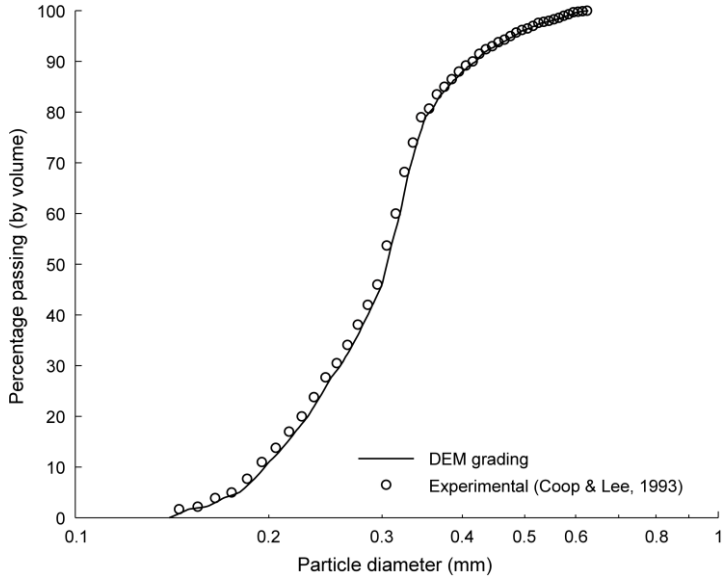

Figure 3 Particle size distribution of the virtual samples used in this study compared with the Ham River sand grading provided by Coop and Lee (1993)

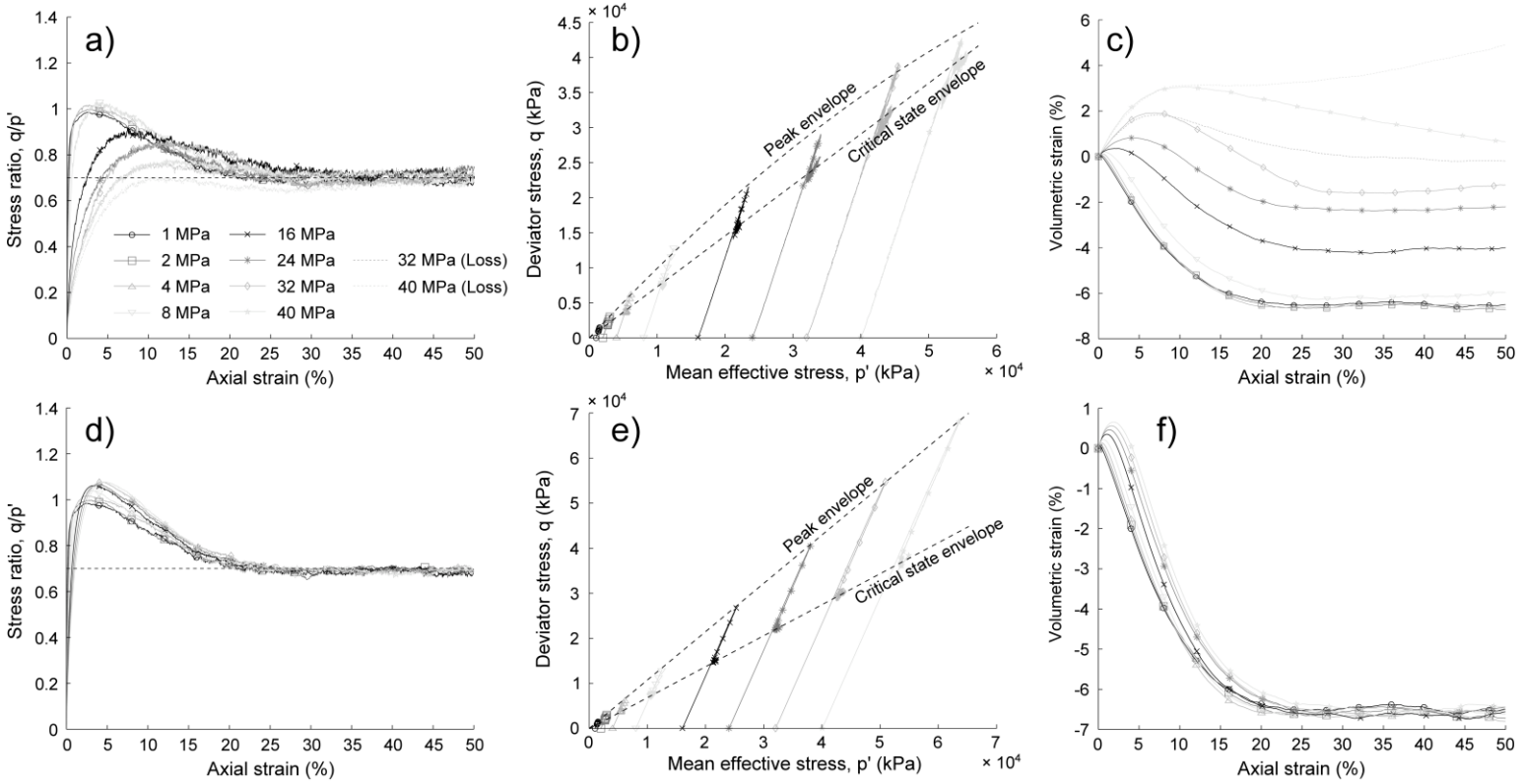

Figure 4 Evolution of stress ratio, q/p', against axial strain (%) (a and d), deviator stress, q, against mean effective stress, p' (both in kPa) (b and e) and volumetric strain against axial strain (c and f). Particle crushing is considered in (a), (b) and (c); it is not in (d), (e) and (f)

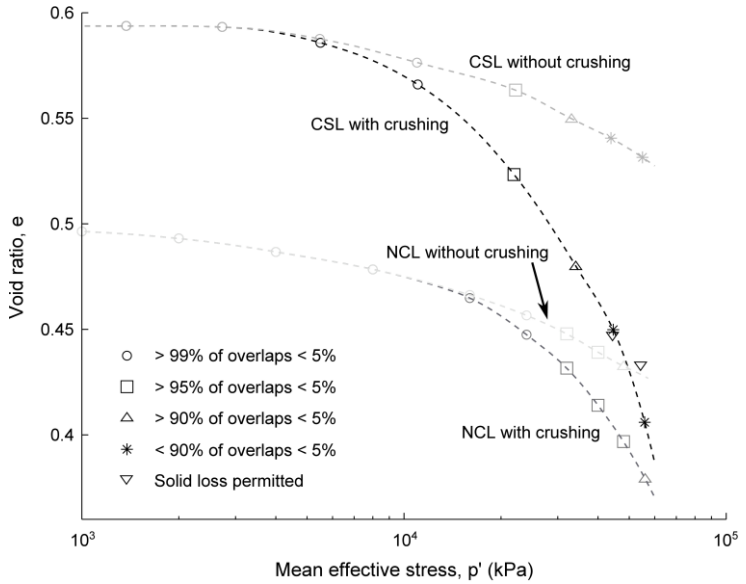

Figure 5 Isotropic normal compression lines (NCL) and critical state lines (CSL) in e–log(p') space. The line markers indicate the interparticle overlaps normalised by the radius of the smaller particle in each contact. The inverted triangular markers correspond to those two simulations in which solid loss is permitted

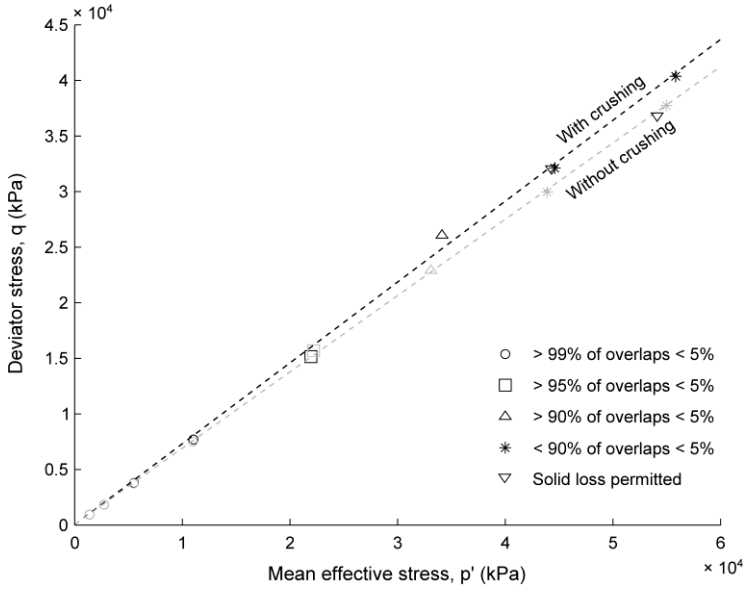

Figure 6 CSLs in *q*–*p′* space both with and without particle crushing. As for Fig. 5, the line markers indicate the interparticle overlaps normalised by the radius of the smaller particle in each contact

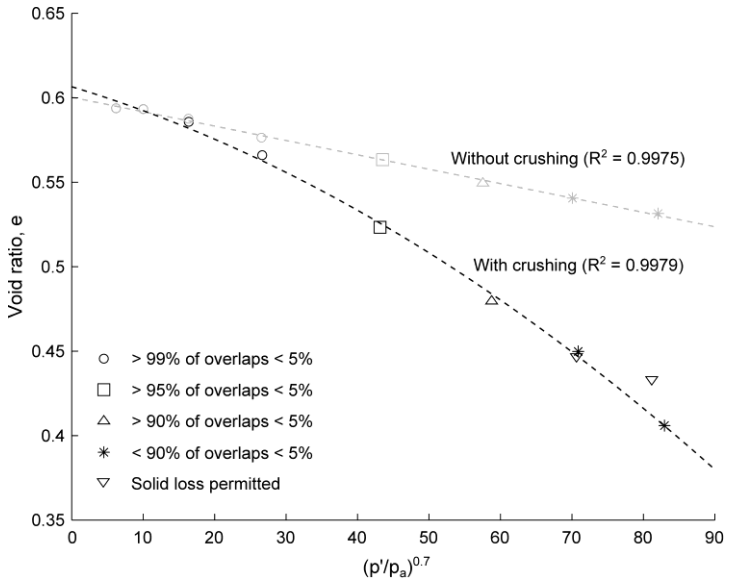

Figure 7 CSLs with and without particle crushing in e–$(p'/p_a)^{\alpha}$ space with $\alpha = 0.7$ (line markers as for Fig. 5)

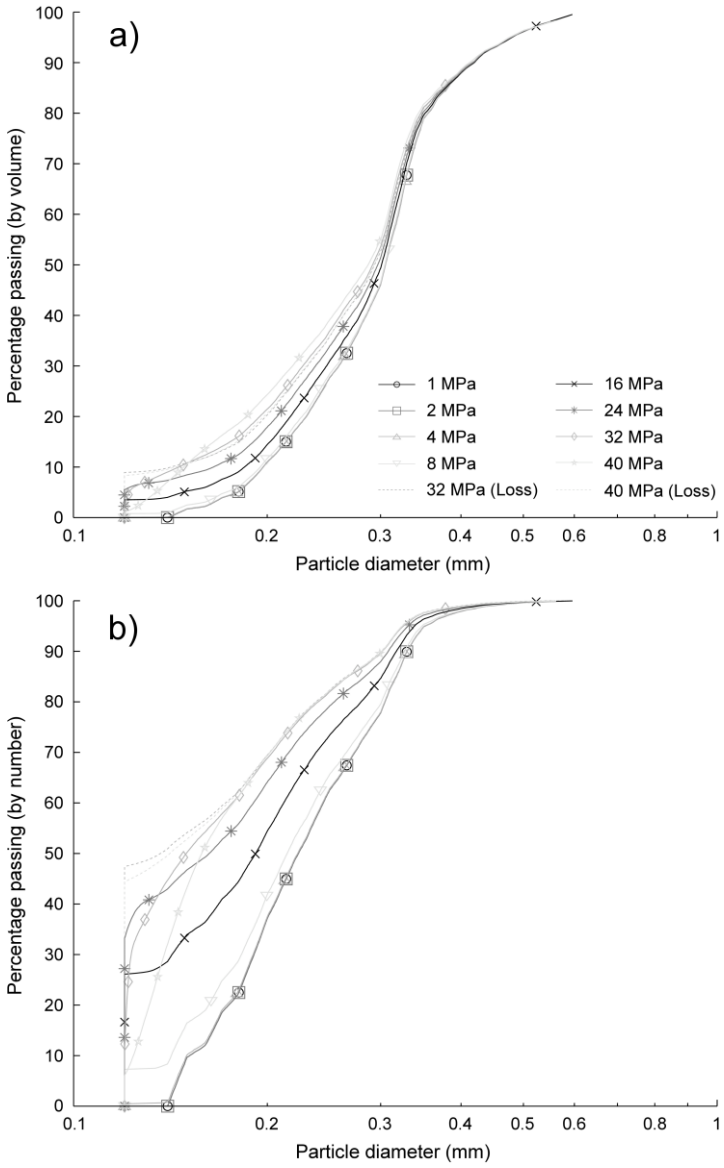

Figure 8 The evolving particle size distribution due to progressive crushing plotted as percentage passing (a) by volume and (b) by number

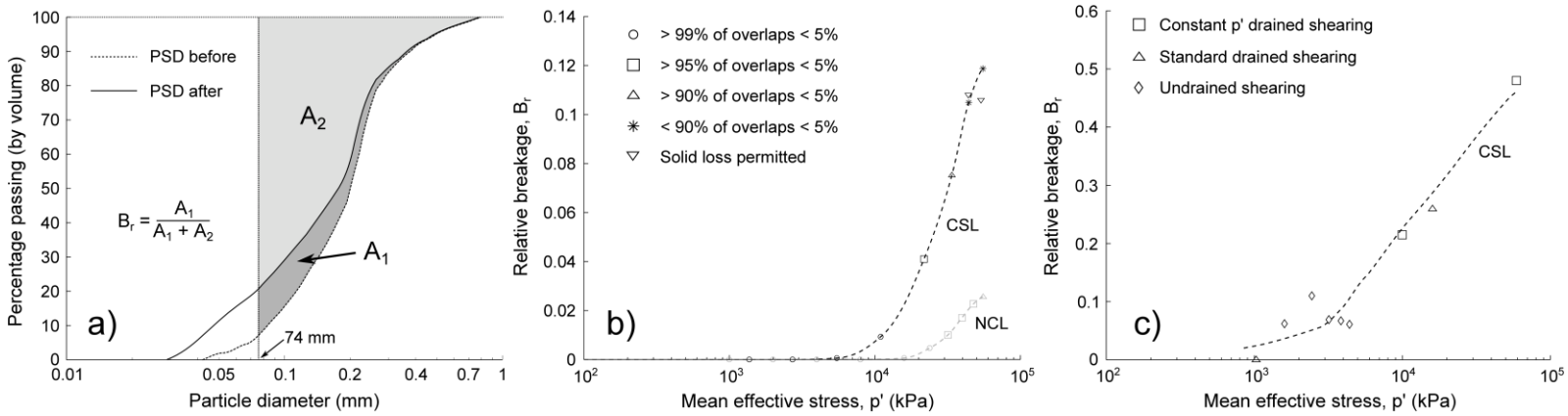

Figure 9 (a) Definition of relative breakage, B_r, as proposed by Hardin (1985); (b) NCL and CSL for the isotropic compression and triaxial shearing simulations, respectively, plotted as B_r against p' (kPa); (c) B_r versus p' for Ham River sand, adapted from Coop (2003)

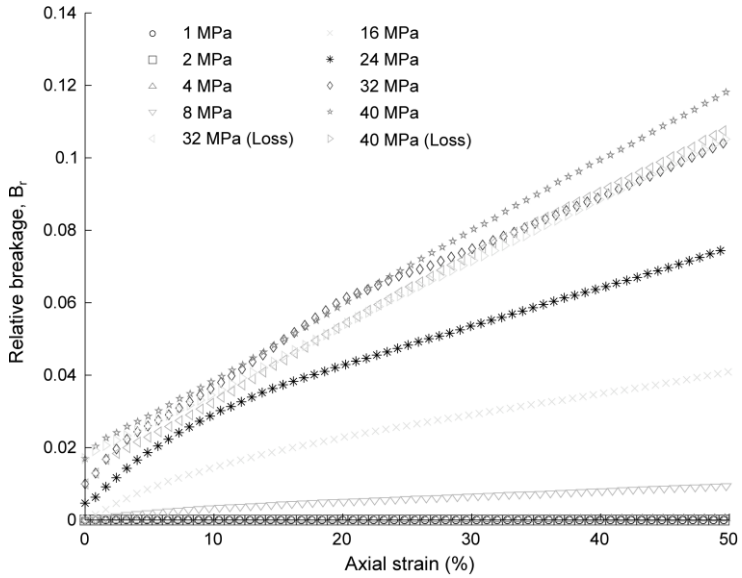

Figure 10 Evolution of relative breakage, B_r, with axial strain (%) during triaxial shearing

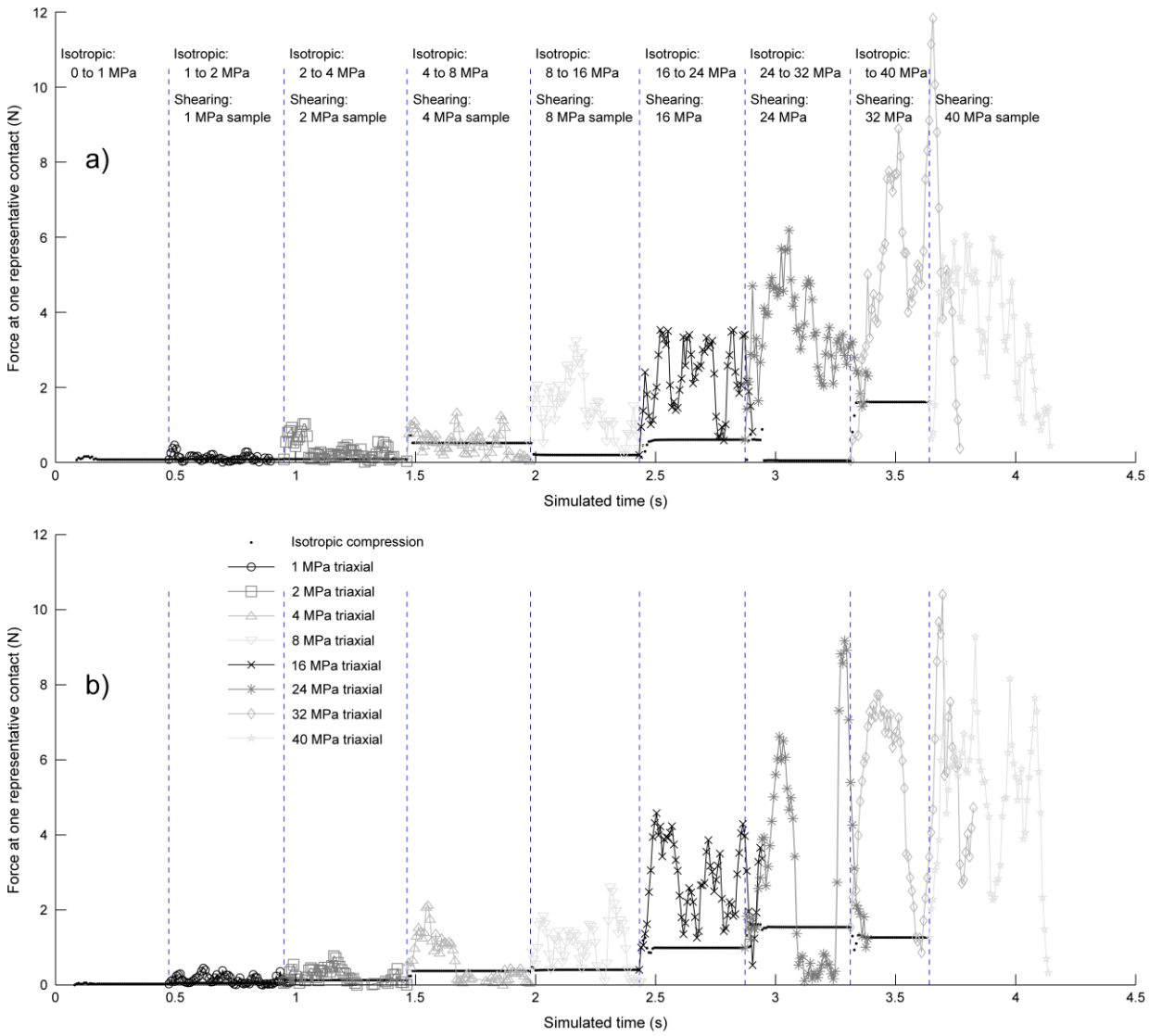

Figure 11

Plots of contact force (N) against simulated time (s) at regularly-spaced output intervals for the entirety of the simulation series considering particle crushing. For each interval considered, both the forces experienced by a representative contact in an isotropic compression simulation and the forces experienced by a representative contact in deviatoric shearing are given. In the case of isotropic compression, the range of stresses over each interval is given and in the case of shearing, the confining pressure is given. Subfigures (a) and (b) correspond to different representative, persistent contacts

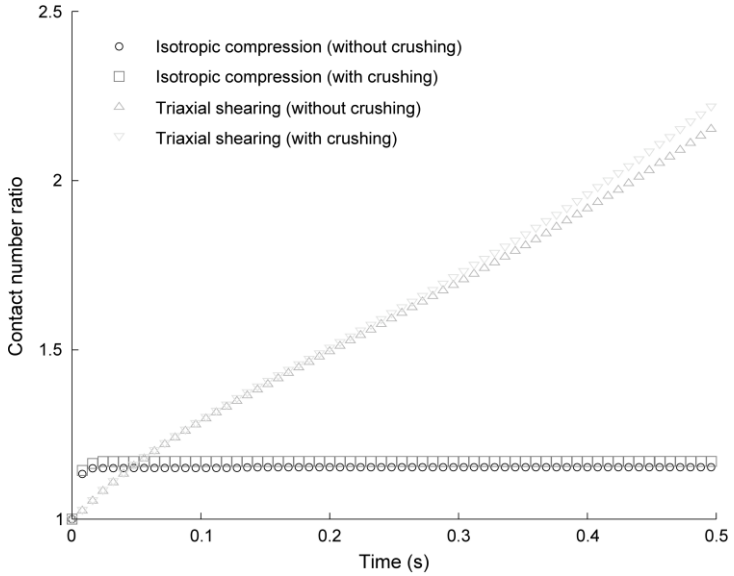

Figure 12 The evolution of contact number ratios, defined according to Eq. (7), against time (s) for four simulations: isotropic compression of an 8 MPa sample to 16 MPa and triaxial shearing of the same 8 MPa sample, both including and disregarding particle crushing in the simulations

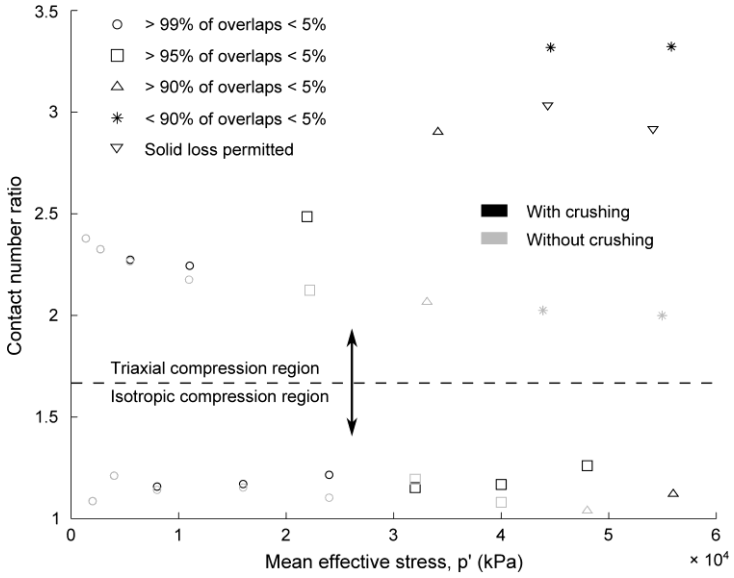

Figure 13 Comparison of contact number ratios against p' (kPa) at the end of each isotropic compression and triaxial shearing simulation

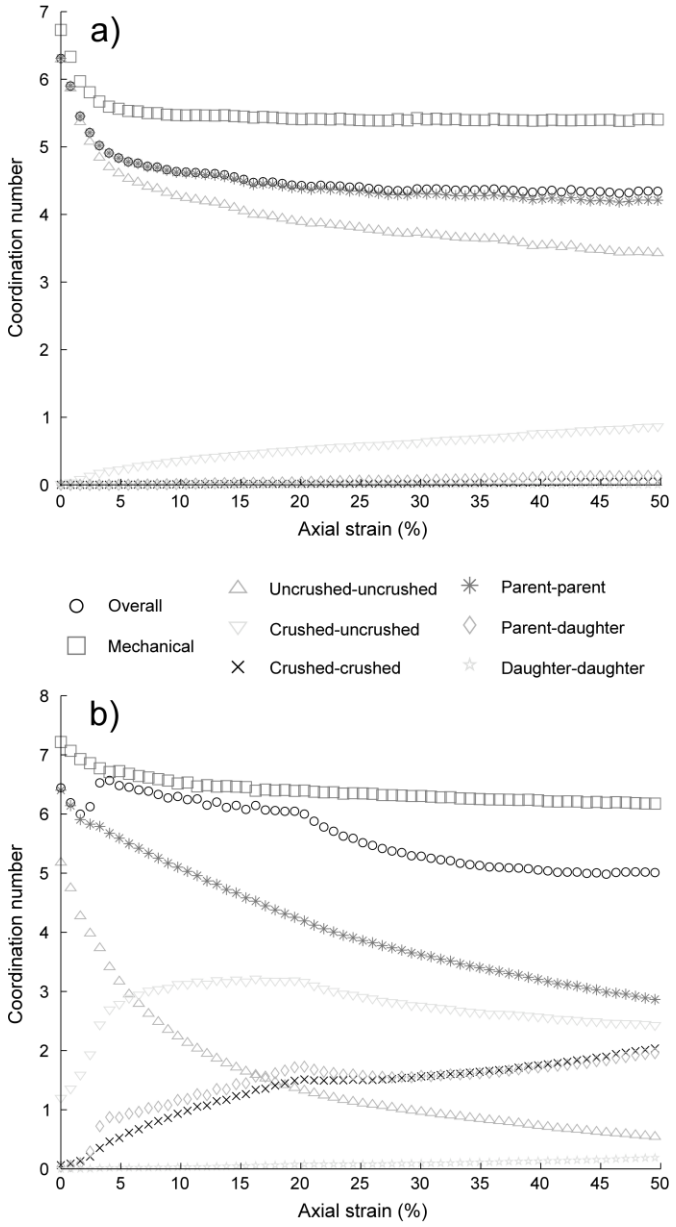

Figure 14 Various definitions of coordination number plotted against axial strain (%) for the simulations including crushing at confining pressures of (a) 8 MPa and (b) 32 MPa